Angular reflectance model for ridged specular surfaces, with comprehensive calculation of inter-reflections and polarization

Dorian Saint-Pierre, Pierre Chavel, Lionel Simonot, Mathieu Hébert

Angular reflectance model for ridged specular surfaces, with comprehensive calculation of inter-reflections and polarization

DORIAN SAINT-PIERRE,[1*] PIERRE CHAVEL[1], LIONEL SIMONOT,[1,2] MATHIEU HEBERT[1]

[1]*Université de Lyon, UJM-Saint-Etienne, CNRS, Institut d Optique Graduate School, Laboratoire Hubert Curien UMR 5516, Saint-Etienne, France*
[2]*Université de Poitiers, Institut Prime UPR CNRS 3346; Futuroscope Chasseneuil, France*
**Corresponding author: dorian.saint.pierre@univ-st-etienne.fr*

Received XX Month XXXX; revised XX Month, XXXX; accepted XX Month XXXX; posted XX Month XXXX (Doc. ID XXXXX); published XX Month XXXX

The color of a surface structured at the mesoscopic scale differs from the one of a flat surface of the same material because of the light interreflections taking place in the concavities of the surface, as well as shadowing effects. The color variation does not only arise in scattering materials, but also in absence of scattering, e.g. in metals and clear dielectrics, just as a consequence of multiple specular reflections between neighboring flat facets of the surface. In this paper, we investigate such color variation in the case of an infinitely long V-shaped groove, having in mind the visual appearance of a surface composed of many structures of that sort, all parallel and identical. We develop a full model of multiple specular reflections, accounting for ray position and orientation and polarization effects occurring at each reflection. We compare that situation with two approximate models, more usual and easier to compute, where light is assumed to remain unpolarized all along, or where the *p*- and *s*-polarized components are treated separately. Spectral reflectances were predicted for various materials and angles of cavities, under diffuse illumination. In most cases, the three models predict very similar bi-hemispherical reflectances, but the hemispherical-directional reflectances can vary noticeably in certain observation directions. This study might help achieving more physically-realistic rendering of dielectric or metallic ridged surfaces in computer graphics.

http://dx.doi.org/10.1364/AO.99.099999

1. INTRODUCTION

It is well known that the structure of surfaces and materials has a crucial influence on the way they reflect light, thereby on their appearance. A same material structured in different ways, under the form of layers or particles, or with different surface topologies, can yield very different appearance attributes, from bright to dark, glossy to matte or transparent to opaque.

The influence of the material structure on appearance is mainly related to the concept of light scattering, which covers a wide variety of optical principles according to the size of the material structures and their arrangement. Regular or periodical structures whose characteristic size is comparable to the wavelength of light generate diffraction, and consequently colorations that are often called structural colors [1]. These effects have been widely explored in optics for more than one century, even though pseudo-periodical structures are still an active subject of investigation [see for example Ref. 2]. In opposition, irregular structures can generate both coherent and incoherent light scattering, which mainly results in a reorientation of light in space and depolarization. For these randomly microstructured materials, many models have also been proposed in the last century to predict their reflection and transmission properties according to the wavelength, polarization, orientation and position of light. Among the most famous theories for the light scattering by volumes, we can mention the Kubelka-Munk model initially introduced for paints [3], the Melamed model for pigments powders and slurries [4], the radiative transfer theory by Chandrasekhar [5], the multi-flux theory, the Van de Hulst works for scattering by particles [6], etc. Beckman and Spizzichino [7] modelled diffraction by surfaces presenting a random roughness. Torrance and Sparrow [8] modelled incoherent reflection by randomly organized microfacets. The most advanced models can take into account the multiple scattering between different facets [9-11]. All these models form a large prediction toolbox for many visual attributes (color, translucency and opacity, gloss and matte aspect), applicable to a wide range of materials according to their optical properties (refractive indices, scattering and absorption coefficients…) and structural properties (surface roughness, particle size and concentration, layer thickness…), provided the material can be considered as homogeneous at the macro- or mesoscopic scale.

For many kinds of surfaces or objects, the multiscale structure of the matter does have to be taken into account in order to obtain accurate optical models and appearance predictions. Describing scattering at multiple scales is generally done by combining different models. The classical literature in physics shows various examples. Mie scattering model is used to describe the light scattering by one particle, and a radiative transfer model is then used to describe the light transport through a volume. For stacks of diffusing layers, the Kubelka-Munk

model describes the light scattering at the microscopic scale within each layer and predicts its reflectance and transmittance, after which the Kubelka layering model [12] or more advanced models describe the flux transfers at the mesoscopic scale between the different layers with their respective interfaces [13-14]. For halftone prints, the optical properties of the paper and the inks can be both modeled by the Kubelka-Munk theory [15], after which the scattering properties of the set of ink dots on top of the paper can be predicted by a number of models describing the flux transfers between the different inked and non-inked areas [16-19]. But models are still missing for a volume made of a 3D juxtaposition of small material elements with different optical properties (e.g., diffuse and transparent ink droplets used in 3D printing), and for a surface whose shape has been given a mesoscopic, possibly periodical structure. The present paper addresses the latter case, when the multiple reflections between the different areas of the non-flat surface give to the object specific reflection properties according to the illumination conditions. We specifically focus periodically ridged surfaces, which enable studying the role of the multiple reflections on their appearance while being rather simple to model with analytical equations. Modeling the appearance of this kind of surface is not only crucial for accurate renderers in computer graphics, but also important in prototyping and manufacturing.

As shown in recent studies dedicated to ridged diffuse materials (ridges with V-profile) [20-21], the presence of periodical ridges modifies the color of the material in comparison to the case where its surface is flat, in different ways according to the ridge shape and the illumination conditions. Specifically, the color of the ridge surface is brighter and more saturated than the one of the flat surface under frontal collimated illumination, but it is darker and less saturated under diffuse illumination. Interreflection models taking explicitly into consideration the microscopic optical properties of the material and the mesoscopic structure of the surface are capable to predict these color variations, thus also allowing the prediction of the irradiance repartition at those two scales.

Recently, three studies, almost concomitant, have addressed the case of nonscattering materials such as metals or clear dielectric materials [10, 11, 22]. They consider surfaces with periodical V-shaped structure as shown in Fig. 1, by assuming that the faces of the ridges are flat, behaving like mirrors. In these three studies, different, although similar analytical expressions are derived for the description of the interreflections, which are in this case a finite number of specular reflections depending on the orientation and position of the incident rays in respect to the illuminated ridges, as well as the angular aperture α of the ridges and the refractive index of the material. The first study, dedicated to computer graphics, presents an analytical model of Bi-directional Reflectance Distribution Function (BRDF) for a distribution of specular V-grooves, the second study, also dedicated to computer graphics, extends the application to anisotropic rough surfaces. The third study, that we authored, focused on the angular radiance perceived from any angle when the surface is illuminated by a completely diffuse light [22]. The three models assume that incident light is unpolarized, as it often is, and remain unpolarized during the whole multiple reflection model.

In the present paper, we propose to model rigorously the polarization of light along the multiple reflection process, in order to see to which extent the approximation made by the previous studies stands according to the considered material, metal or dielectric. We compare this rigorous model with two approximate models where light is assumed to remain unpolarized all along (*first approximate model*), or where the *p*- and *s*-polarized components are treated separately (*second approximate model*). Notice that we assume that the facets are large enough, e.g. larger than a few tens of micrometers, to prevent visible effects of diffraction, which would be inevitable with such periodically structured facets if they were smaller.

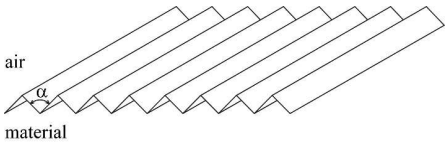

Fig. 1 – Structured surface with parallel, periodical, and identical V-shaped ridges of dihedral angle α.

The paper is organized as follows: we firstly introduce in Section 2 the formalization of multiple light reflections in a V-cavity with specular facets, and derive in Section 3 the analytical formulas describing the attenuation of the radiance along its path into the cavity, according to the three models. Then, in Section 4, we sum up the radiances in order to obtain hemispherical-directional and bi-hemispherical reflectances. Predictions are made with various materials, including a dielectric, a semi-conductor, and metals, in order to study the influence of the surface shape (precisely the dihedral angle of the cavities) on their respective spectral reflectances and their color. The differences between the predictions given by the three models are compared. Section 5 finally draws the conclusions.

2. MULTIPLE REFLECTIONS OF A LIGHT RAY IN A SPECULAR CAVITY

First of all, we can notice from Fig. 1 that a light ray entering into one cavity is reflected, possibly multiple times, in this cavity only. Therefore, we can focus on the reflection of light by one cavity, and consider that all cavities reflect light in the same way. In this section, we analytically predict the amount and directions of light reflected by the cavity. The model is based on geometrical optics, and therefore ray tracing. It describes the path of light after the successive reflections across the structure, and takes into account the number of bounces.

2.1 Geometry of the cavity

Each cavity is formed by two specular facets of infinite length along the *x* axis of the 3D Cartesian space (Fig. 2). The width of both facets is set to unity (it could be equivalently any other value: the width has no impact on the interreflection phenomenon as shown in [20] and on the computation of the specular radiance that we want to perform here). The dihedral angle between the two facets is denoted as α. Hence, each facet forms a dihedral angle $\alpha/2$ with the *(xOz)*-plane, where the *z*-axis corresponds to the normal of the average structured surface.

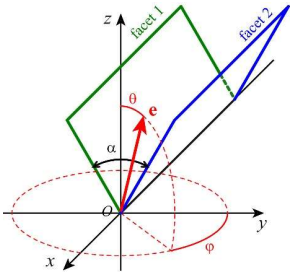

Fig. 2 – 3D geometry of one cavity, and vector **e** representing the direction of illumination.

The normal of facets 1 and 2 are respectively:

$$\mathbf{N_1} = \left(0,\ \cos(\alpha/2),\ \sin(\alpha/2)\right) \quad (1)$$

and

$$\mathbf{N_2} = \left(0,\ -\cos(\alpha/2),\ \sin(\alpha/2)\right) \quad (2)$$

The incident light ray is characterized by a unit radiance, and a unit vector **e** with spherical coordinates (θ, φ) represented in Fig. 2. In this Cartesian coordinate system, the vector **e** is given by:

$$\mathbf{e} = (\sin\theta\sin\varphi,\ \sin\theta\cos\varphi,\ \cos\theta) \quad (3)$$

2.2 Multiple reflections in a cavity

Once a light ray enters into a cavity, it may undergo one or several successive reflections on the facets. After each reflection, the direction of the ray is modified according to Snell's laws. However, in geometrical optics, it is classical to unfold the rays into their virtual prolongation, which is aligned with the incident ray, as shown on Fig. 3a through the example of two rays.

By using this representation for the cavity, the path of one ray is represented by a straight line crossing the successive images of the facets: after a reflection on facet 1, the ray reaches the image of facet 2 (which forms an angle α with facet 1), then the image of facet 1 (which also forms an angle α with the image of facet 2), and so on.

2.3 Number of reflections within the cavity

The number of reflections within the cavity depends on both orientation and position of the ray. This is visible in Fig. 3, where the two rays are parallel (thus characterized by the same vector **e**) and strike facet 2 in different positions: one ray (represented in red; color version online) undergoes 4 reflections, whereas the other ray (represented in orange) undergoes 3 reflections. The ray light paths in broken straight lines are featured on Fig. 3b, in a projection onto the (*y0z*) plane of the 3D scene represented on Fig. 3a. In the (*y0z*) plane, the projection of vector **e**, denoted as $\mathbf{e}^{\perp}$, is:

$$\mathbf{e}^{\perp} = (\sin\theta',\ \cos\theta') \quad (4)$$

with

$$\theta' = \arctan\left(\tan\theta\cos\varphi\right) \quad (5)$$

The number of reflections according to the orientation and position of the ray is computed according to the following geometrical considerations, in the (*y0z*) plane. The orientation of the ray is denoted by the angle θ′ given by Eq. (4). Its position is described by the point *P* where the ray meets the line (AB) which joins the extremities of the facets in the (*y0z*) plane, drawn in Fig. 3c. This point *P* has the coordinates $P = \left(y_P, \cos(\alpha/2)\right)$. The ray meets the unit circle centered in point $O = (0,0)$ in two points: first in point $G = \left(\sin\beta_G, \cos\beta_G\right)$, then in point $H = \left(\sin\beta_H, \cos\beta_H\right)$.

Fig. 3 shows two examples for the same position y_P but two different orientations of the ray. In Fig. 3c, the ray strikes first facet 1, in Fig. 3d, it strikes first facet 2. The facet first met is determined by the following condition: if the meeting point $Q = \left(y_Q, 0\right)$ of the ray and the *y*-axis has a negative abscissa y_Q, facet 1 is met first, otherwise, facet 2 is met first. With some geometric calculations, we find that abscissa y_Q is given by

$$y_Q = \frac{\sin\left(\beta_H - \beta_G\right)}{\cos\beta_G - \cos\beta_H} \quad (6)$$

where the angles β_G and β_H are computed as follows.

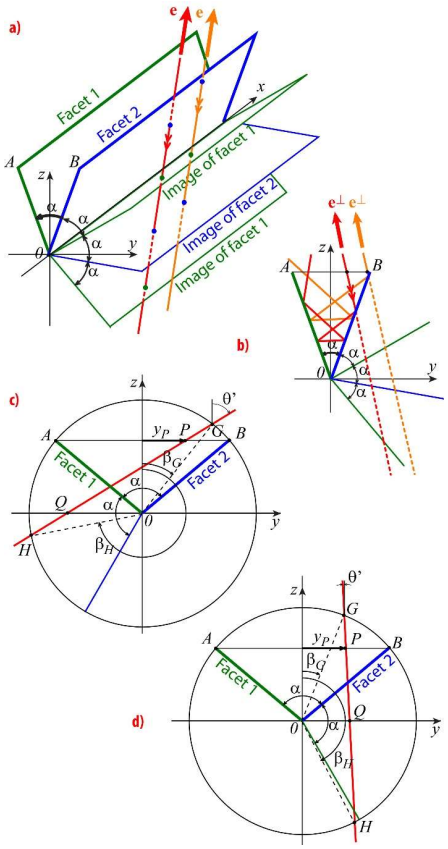

Fig. 3 – **a-b)** Representations of two light rays parallel to the unit vector **e,** striking the cavity on facet 2 in different positions. **b)** 2D representation of the two same light rays projected onto the (*y0z*) vertical plane. The light path can be represented by a straight line joining the successive images of the facets. The projection of the real light paths in broken straight lines is also represented. Geometry for the calculation of the number of reflections, for a same position y_P of the ray, and two different orientations. **c-d)** Geometry for the calculation of the number of reflections, for a same position y_P of the ray, and two different orientations.

Since

$$\mathbf{PG} = \left(\sin\beta_G - y_P,\ \cos\beta_G - \cos\left(\tfrac{\alpha}{2}\right)\right)$$

and $\mathbf{e}^{\perp}$ are collinear, we have:

$$\det\begin{pmatrix} \sin\beta_G - y_P & \sin\theta' \\ \cos\beta_G - \cos\left(\frac{\alpha}{2}\right) & \cos\theta' \end{pmatrix} = 0 \quad (7)$$

After some calculations, Eq. (7) can be written

$$\sin(\beta_G - \theta') = y_P \cos\theta' - \cos\left(\frac{\alpha}{2}\right)\sin\theta' \quad (8)$$

and by noticing that $\beta_G - \theta' < \pi/2$, we obtain

$$\beta_G = \theta' + \arcsin\left[y_P \cos\theta' - \cos\left(\frac{\alpha}{2}\right)\sin\theta'\right] \quad (9)$$

Likewise **PH** and $\mathbf{e}^{\perp}$ are collinear, and by following similar reasoning as above with point *H* in place of point *G*, therefore with angle β_H in place of β_G, we obtain:

$$\sin(\beta_H - \theta') = y_P \cos\theta' - \cos\left(\frac{\alpha}{2}\right)\sin\theta' \quad (10)$$

This time, we can notice that $\beta_H - \theta' > \pi/2$, therefore we have:

$$\beta_H = \theta' + \pi - \arcsin\left[y_P \cos\theta' - \cos\left(\frac{\alpha}{2}\right)\sin\theta'\right] \quad (11)$$

Figs. 3c and 3d illustrates the fact that the ray strikes first facet 1 when $y_Q < 0$, and strikes first facet 2 when $y_Q > 0$. Finally, the number of reflections occurring after the first reflection of the first facet met is the number of times angle $\gamma_H - \alpha/2$ contains α. By introducing the angle γ_H defined as:

$$\gamma_H = \begin{cases} 2\pi - \beta_H \text{ when } y_Q < 0 \\ \beta_H \text{ when } y_Q > 0 \end{cases} \quad (12)$$

the total number of reflections is given by:

$$m = \text{floor}\left[\frac{\gamma_H}{\alpha} - \frac{1}{2}\right] + 1 \quad (13)$$

where symbol floor[...] denotes the integer part of the number in argument.

3. RADIANCE ATTENUATION FOR ONE RAY

Now that the number of light reflections has been determined, we can express the global attenuation undergone by the radiance attached to a given light ray. We first present a simple approximate model which considers that light remains unpolarized after all reflections. Then, present a second approximate model where we consider the *s* and *p* components separately, and we finally introduce the rigorous model where the evolution of the polarization state after each reflection is rigorously modeled.

3.1 First approximate model: light remaining unpolarized

Let's consider an unpolarized light ray reflected on an interface between a first medium, in our case always air, and a second medium. It is coming from the first medium with a local incidence angle θ_i. The reflectance, denoted as $R(\theta_i)$, is the average of the squared modules of the Fresnel coefficients for the *s* (perpendicular) and *p* (parallel) components [23]:

$$R(\theta_i) = \frac{1}{2}\left(\left|r_P(\theta_i)\right|^2 + \left|r_S(\theta_i)\right|^2\right) \quad (14)$$

Then, by multiplying the successive Fresnel reflectances $R(\theta_i)$ corresponding to the different reflections on facets, we obtain the total reflectance for one path of the light. Note that we ignore the part of the light transmitted into the material (we can consider that it is absorbed, as it is the case for metals and dark dielectrics).

For each reflection, we compute the local incidence angle θ_i. It can be easily obtained through the dot product between vector **e**, which describes the direction of the ray, and the normal of the facet, or image of facet, on which the considered reflection occurs.

The facets have the normal vectors $\mathbf{N}_1$ and $\mathbf{N}_2$ given by Eq. (1). The local incident angle for the first reflection depends on whether the ray first meets facet 1 or facet 2, therefore on the sign of the parameter y_Q defined by Eq. (6):

$$\theta_i^{(1)} = \begin{cases} \arccos(\mathbf{e}\cdot\mathbf{N}_1) & \text{if } y_Q < 0 \\ \arccos(\mathbf{e}\cdot\mathbf{N}_2) & \text{if } y_Q > 0 \end{cases} \quad (15)$$

where symbol "$\cdot$" denotes the dot product.

The next reflections, if any, occur on images of facets whose normal vector are denoted as $\mathbf{N}_1^{(j)}$ or $\mathbf{N}_2^{(j)}$ if the first reflection occurs on facet 1, respectively on facet 2. These normal vectors, for $j = 1$ to the number of reflections *m* given by Eq. (13), are given by:

$$\mathbf{N}_1^{(j)} = \begin{pmatrix} 0 \\ \cos(\alpha/2 + (j-1)\alpha) \\ \sin(\alpha/2 + (j-1)\alpha) \end{pmatrix} \quad (16)$$

and

$$\mathbf{N}_2^{(j)} = \begin{pmatrix} 0 \\ -\cos(\alpha/2 + (j-1)\alpha) \\ \sin(\alpha/2 + (j-1)\alpha) \end{pmatrix} \quad (17)$$

and the local incident angle is given by

$$\theta_i^{(j)} = \begin{cases} \arccos(\mathbf{e}\cdot\mathbf{N}_1^{(j)}) & \text{if } y_Q < 0 \\ \arccos(\mathbf{e}\cdot\mathbf{N}_2^{(j)}) & \text{if } y_Q > 0 \end{cases} \quad (18)$$

Finally, the global attenuation of the radiance according to its position y_P between $-\sin(\alpha/2)$ and $\sin(\alpha/2)$, and its orientation (θ,φ), is given by the reflectance:

$$R(\theta,\varphi,y_P) = \prod_{j=1}^{m} R\left[\theta_i^{(j)}\right] \quad (19)$$

Notice that according to the Helmholtz reciprocity principle, a ray following the same path within the cavity but in opposite direction would undergo exactly the same attenuation. Hence, $R(\theta,\varphi,y_P)$ can denote the attenuation for the ray entering or exiting the cavity at the angle (θ,φ) through the position y_P.

3.2 Second approximate model: reflections of p and s polarization components, separately

Regarding the polarization of light along the multiple reflection process within the cavity, we can think in a second approximate model, by assuming that the *p* and *s* polarized components of the incident light (half the total radiance for each one) follow the same multiple reflection process. We can formulate the approximation that they do it in parallel. The *p*-polarized light component remains *p*-polarized after each reflection (therefore vibrating alongside each successive incidence plane), and the *s*-polarized light component remains *s*-polarized (therefore vibrating perpendicularly to each successive incidence plane). The model is similar to the first approximate model, except that Eq. (19) is computed twice, a first time by substituting the Fresnel reflectance for unpolarized light, $R\left[\theta_i^{(j)}\right]$, with the one for *p*-polarized light, $R_p\left[\theta_i^{(j)}\right]$, and a second time by substituting $R\left[\theta_i^{(j)}\right]$ with the Fresnel reflectance for *s*-polarized light, $R_s\left[\theta_i^{(j)}\right]$. Two reflectance components are obtained, $R_p(\theta,\varphi,y_P)$ and $R_s(\theta,\varphi,y_P)$, and their average forms the total reflectance:.

$$R(\theta,\varphi,y_P) = R_p(\theta,\varphi,y_P) + R_s(\theta,\varphi,y_P) \quad (20)$$

Supprimé: (7)

Mis en forme : Police :(Par défaut) Cambria, 9 pt, Non Gras, Condensé de 0.4 pt

Supprimé: (13)

Mis en forme : Police :Cambria, 9 pt, Non Gras

Supprimé: (19)

3.3 Rigorous model: calculating the polarization of light along the multiple reflection process

The multiple reflections occurring in the cavity bring to the fore the question of the polarization of the light. Even if the light source is incoherent and unpolarized, each reflection partially polarizes the light. It is necessary to rigorously develop the calculation describing the transformation of the polarization and more precisely of its two components *s* (perpendicular to the incidence plane on the current facet) and *p* (parallel to it). That enables us to better apprehend the influence of the polarization on the final reflectance of the surface.

Let us compute the Fresnel reflection coefficients for both the *s* and *p* components of light. Remind that at each reflection on a facet, or equivalently, at each intersection of the light ray with the images of the V-cavity facets as shown on Fig. 3, the incidence plane changes.

At first, the incident wave is represented by its electric field of amplitude E_0. Because it varies very rapidly in a random manner, this wave is said to be incoherent and unpolarized. It can be represented by the sum of two wave components which are temporally decorrelated, vibrating perpendicularly to each other, and of respective amplitudes E_{0p} and E_{0s} [23].

After their reflection on the first facet, we have:

$$\begin{cases} E_{1p} = r_{1p} E_{0p} \\ E_{1s} = r_{1s} E_{0s} \end{cases} \quad (21)$$

which is more conveniently written in matrix form

$$\begin{pmatrix} E_{1p} \\ E_{1s} \end{pmatrix} = \mathbf{R_1} \begin{pmatrix} E_{0p} \\ E_{0s} \end{pmatrix} \quad (22)$$

where

$$\mathbf{R_1} = \begin{pmatrix} r_{1p} & 0 \\ 0 & r_{1s} \end{pmatrix} \quad (23)$$

The wave components of amplitude E_{1p} and E_{1s} are respectively vibrating parallel and perpendicular to the incidence plane 1, and then arrive on facet 2. Notice that the incidence plane related to facet 2, labeled 2, differs from the incidence plane 1 previously considered: they form a dihedral angle, denoted as ψ_{12}, that will be computed later.

In this incidence plane 2, the new wave components of amplitude E'_{1p} and E'_{1s}, whose vibration directions are respectively parallel and perpendicular to the new incidence plane, can be derived from the previous amplitudes E_{1p} and E_{1s}, and are given by:

$$\begin{cases} E'_{1p} = E_{1p}\cos\psi_{12} + E_{1s}\sin\psi_{12} \\ E'_{1s} = -E_{1p}\sin\psi_{12} + E_{1s}\cos\psi_{12} \end{cases} \quad (24)$$

If we now use the following rotation matrix:

$$\mathbf{M}(\psi_{12}) = \begin{pmatrix} \cos\psi_{12} & \sin\psi_{12} \\ -\sin\psi_{12} & \cos\psi_{12} \end{pmatrix} \quad (25)$$

and the diagonal matrix containing the Fresnel reflection coefficients:

$$\mathbf{R}_2 = \begin{pmatrix} r_{2p} & 0 \\ 0 & r_{2s} \end{pmatrix} \quad (26)$$

we can then write

$$\begin{pmatrix} E_{2p} \\ E_{2s} \end{pmatrix} = \mathbf{R}_2\mathbf{M}(\psi_{12}) \begin{pmatrix} E_{1p} \\ E_{1s} \end{pmatrix} = \mathbf{R}_2\mathbf{M}(\psi_{12})\mathbf{R}_1 \begin{pmatrix} E_{0p} \\ E_{0s} \end{pmatrix} \quad (27)$$

Iterating for the *m* reflections, we obtain:

$$\begin{pmatrix} E_{mp} \\ E_{ms} \end{pmatrix} = \mathbf{R}_m\mathbf{M}(\psi_{m-1,m})...\mathbf{R}_3\mathbf{M}(\psi_{23})\mathbf{R}_2\mathbf{M}(\psi_{12})\mathbf{R}_1 \begin{pmatrix} E_{0p} \\ E_{0s} \end{pmatrix} \quad (28)$$

We thus have

$$\begin{cases} E_{mp} = aE_{0p} + bE_{0s} \\ E_{ms} = cE_{0p} + dE_{0s} \end{cases} \quad (29)$$

where *a*, *b*, *c*, *d* are the resulting entries of the matrix product in (28).

By using the fact that the two incident wave components of amplitudes E_{0p} and E_{0s} are temporally decorrelated, we can write the flux F_{mp} and F_{ms} attached to them as:

$$\begin{aligned} F_{mp} &= a^2F_{0p} + b^2F_{0s} = (a^2 + b^2)F_0/2 \\ F_{ms} &= c^2F_{0p} + d^2F_{0s} = (c^2 + d^2)F_0/2 \end{aligned} \quad (30)$$

where F_0, F_{0p} and F_{0s} are the fluxes attached to the incident wave and its *p* and *s* components.

Finally, the total reflected flux is:

$$F_m = F_{mp} + F_{ms} = (a^2 + b^2 + c^2 + d^2)\frac{F_0}{2} \quad (31)$$

The last missing point in the description of the model is the computation of the dihedral angles ψ_{12}, ψ_{23}, etc. In the geometrical configuration we considered in Fig. 3, the direction of propagation of the ray in the whole reflection process is given by vector **e**, Eq. (3). It is contained in the incidence plane *j* (*j* = 1, ..., m) with the normal $\mathbf{N}_k^{(j)}$ of the facet *k* = 1, 2. Hence, the normal vector of the incidence plane *j*, denoted as $\mathbf{S}_j$, is collinear to $\mathbf{e}\times\mathbf{N}_k^{(j)}$, where symbol × denotes the cross product operator:

$$\mathbf{S}_j = \frac{\mathbf{e}\times\mathbf{N}_k^{(j)}}{\left\|\mathbf{e}\times\mathbf{N}_k^{(j)}\right\|} \quad (32)$$

Since the dihedral angle $\psi_{j,j+1}$ between the two planes of incidence is also the angle between their normal vectors, we have:

$$\cos\psi_{j,j+1} = \left|\mathbf{S}_j \cdot \mathbf{S}_{j+1}\right| \quad (33)$$

4. REFLECTANCE OF THE STRUCTURED SURFACE

From the reflectance attached to each incident radiance within the cavity, we could derive the BRDF of a ridged surface whose topology would be made of a juxtaposition of identical V-cavities. However, as the surface contains only two facet orientations, the BRDF is not interesting to display: it is simply a sum of Dirac Delta functions, the number of these functions corresponding to the maximum number of reflections for the considered incident angle. Instead of BRDF, we propose to derive the directional-hemispherical reflectance of the structured surface for a directional illumination in a given direction (θ, φ) and a collection of light over the hemisphere. This reflectance is equal to the hemispherical-directional reflectance based on a geometric configuration where the illumination is Lambertian over the hemisphere, and the observer is placed in direction (θ, φ). Finally, by integrating the hemispherical-directional reflectance over the hemisphere, we obtain the bi-hemispherical reflectance [24].

4.1 Directional-hemispherical reflectance

Let us consider that the cavity is illuminated by directional light from a direction (θ,φ) over a band joining the two edges of the cavity, of length $2\sin(\alpha/2)$ along the *y* axis and of width Δx along the *x* axis. We assume that same radiance L_i strikes each point of the band, which therefore receives a uniform irradiance

$$E_i = L_i \cos\theta \Delta\omega \quad (34)$$

where $\Delta\omega$ denotes the small solid angle of illumination. Since the illuminated area is $2\sin(\alpha/2)\Delta x$, the incident flux on the band is $F_i = 2\sin(\alpha/2)\Delta x E_i$. On each elementary area within the band, centered around the position y_p and of size $\Delta x dy_p$, the elementary flux is $dF_i = \Delta x dy_p E_i$.

The different elementary fluxes are reflected in various directions according to the facet that each one meets first and the number of reflections. By collecting the whole reflected flux, in practice with a measurement device equipped with an integrating sphere, the captured flux F_r is given by

$$F_r = \Delta x E_i \int_{y_p=-\sin(\alpha/2)}^{\sin(\alpha/2)} R(\theta,\varphi,y_p)\,dy_p \quad (35)$$

The directional-hemispherical reflectance of the band associated with this orientation of the incident light, and by extension of the whole structured surface made of a juxtaposition of identical bands, is therefore:

$$R(\theta,\varphi) = \frac{F_r}{F_i} = \frac{1}{2\sin(\alpha/2)} \int_{y_p=-\sin(\alpha/2)}^{\sin(\alpha/2)} R(\theta,\varphi,y_p)\,dy_p \quad (36)$$

4.2 Hemispherical-directional reflectance

According to the reverse path principle, this directional-hemispherical reflectance $R(\theta,\varphi)$ is also the hemispherical-directional reflectance, corresponding to the measurement geometry where the surface is observed from the direction (θ,φ) and illuminated by Lambertian light. This geometry is the one that we will consider later in our simulations, as it is more consistent with practical observation scenarios, for example a grooved surface placed under a forecast sky and visually observed from any direction. The picture in Fig. 4 shows an example of a V-cavity made of gold with a dihedral angle of 45°, placed in an integrating sphere in order to have a Lambertian illumination, and observed from a direction ($\theta \approx 30°$, $\varphi \approx 90°$). On the top of the picture, near the edge of the cavity, we see the different images of each facet by the other one. As the number of reflections increase, the color looks darker and more saturated, an effect that will be studied in more details in the next sections. We also concretely see what was suggested by Fig. 3: the number of reflections varies according to the position into the cavity, along the *y* axis defined in Fig. 2. The red rectangle drawn on the picture represents the area where the cavity can be considered as a cavity of infinite length, without edge effects. The hemispherical-directional reflectance given by Eq. (36), and its related color, correspond to the average reflectance, respectively average color, captured over this area.

In this hemispherical-directional geometry, the specular reflections on the facets do not modify the geometrical extent of the rays; the radiance L_r perceived in one direction (θ,φ) is therefore:

$$L_r(\theta,\varphi) = R(\theta,\varphi) L_i \quad (37)$$

It is possible to display the reflectance given by Eq. (36) according to the observation direction on a 2D map thanks to the Lambert azimuthal equal area projection [25]. To every direction (θ,φ) corresponds a point (u,v) within a disk of radius $\sqrt{2}$ whose coordinates are given by:

$$\begin{cases} u = 2\sin(\theta/2)\cos\varphi \\ v = 2\sin(\theta/2)\sin\varphi \end{cases} \quad (38)$$

The advantage of this transformation is that it conserves the areas by mapping a portion of the hemisphere of a given area into a portion of the disk with same area, as illustrated by Fig. 5.

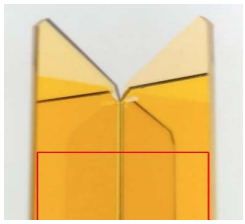

Fig. 4 – RGB picture of a V-cavity made of gold with dihedral angle of 45°, placed in an integrating sphere and observed from a direction ($\theta \approx 30°$, $\varphi \approx 90°$). The red rectangle features the area where the cavity can be considered as a cavity of infinite length.

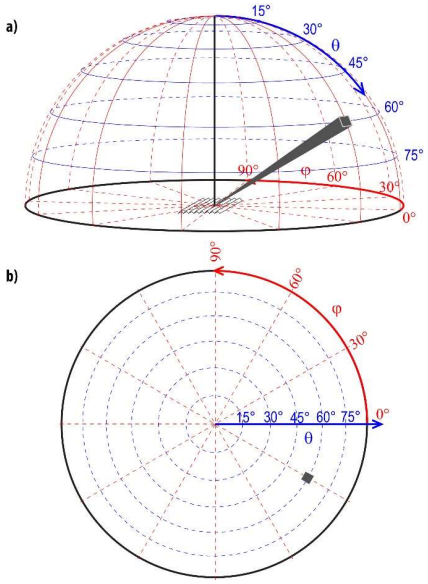

Fig. 5 – When the hemisphere (a) is mapped onto a disk (b) according to the Lambert azimuthal equal area projection, any portion of the hemisphere with area *A* is mapped into a portion of the disk with same area *A*.

In order to apprehend the change in reflectance and color due to the dihedral angle of cavity and/or the viewing angle, we computed the hemispherical-directional reflectance by using the rigorous model presented in Section 3.3 in Eq. (36), for each wavelength of the light from 380 nm to 730 nm in steps of 10 nm, for different materials, and different dihedral angle values: 180° (flat surface), 150°, 120°, 90°, 60° and 45°. The materials are opaque black glass (refractive index assumed to be 1.5), and materials whose spectral complex refractive indices have been found in the database refractiveindex.info: silicon, a semi-conductor with a behavior similar to a dielectric material in the visible range, and pure metals: gold, silver, copper, and aluminum. Silicon is an interesting study case; the real part of its refractive index in the visible spectrum is very high (around 4) and the imaginary part is

low. Since the gap between the two polarizations for this material can be high, it is the best example to study the influence of the polarization model used on the reflectance of the structured surface. For each observation direction (i.e., each point in a map), the spectral reflectance computed is converted first into CIE 1931 XYZ tristimulus values by considering a D65 illuminant, then, for a better visualization, into L*a*b* color values by considering a perfectly white diffuser under the same illuminant as white reference for the chromatic adaptation. We finally convert these L*a*b* values into sRGB color values in order to obtain displayable digital images. The color maps thus generated are shown in Fig. 6.

In addition to the color maps, we computed maps of the maximum number of reflections for each observation direction. In directions where the captured light has undergone one reflection, whatever its entrance position in the cavity is, the corresponding point of the map is colored in light grey (area labeled 1). Other colors for labels 2, 3 and 4 are used when the captured light is subject to have undergone 2, 3 or 4 reflections, respectively.

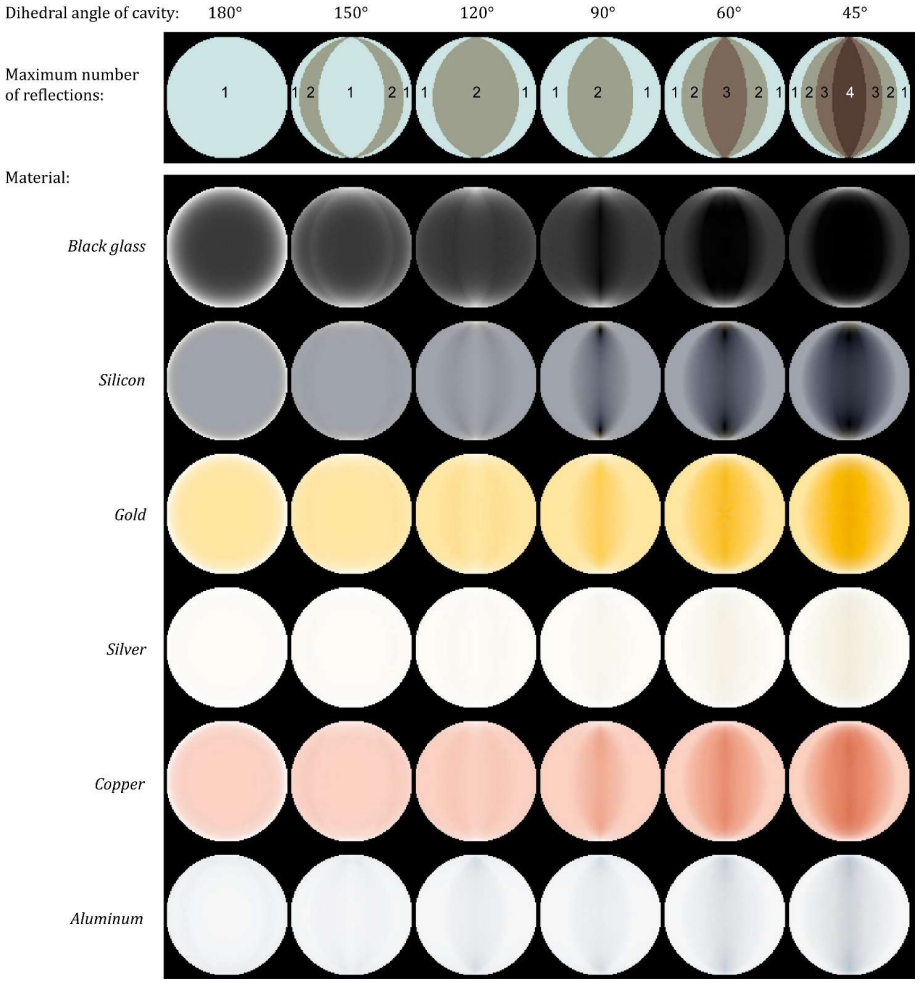

Fig. 6 – Color maps of hemispherical-directional reflectance for various materials, obtained with different dihedral angle of cavity, represented with the Lambert azimuthal equal area projection.

By observing the color maps related to the dielectric material (black glass) in Fig. 6, we can see that the reflectance is globally very weak, except at grazing incidence angles (periphery of the disks) when the cavity dihedral angle is large (reflectance reaches 1 at these grazing angles in the case of the flat surface, i.e., when α = 180°). This is coherent with the angular variation of the Fresnel reflectance. For other dihedral angles of the cavity, the highest reflectance peaks are located near the zones where the azimuthal angle $\varphi = \pi/2$, i.e., when the incident plane contains the *x*-axis, directions where the appearance relief of the cavity is the lowest. We can also distinguish some discontinuities in the maps, which correspond to the directions at which the number of reflections within the cavity is incremented by one. For example, on the map attached to an aperture of 90°, a central area is lighter than the rest of the graph: it corresponds to rays undergoing one reflection, whereas in the rest of the graphs, rays undergo two reflections. Since the Fresnel reflectance at non-grazing incidence angles is low (less than 0.05 under 45° of incidence), radiance trends rapidly toward zero as the number of reflections increases.

For silicon, a semi-conductor with high refractive index but low extinction coefficient in the visible spectrum of light, the influence of the surface structure is similar as the one observed with black glass, but amplified. It looks darker in direction where the number of reflections in the cavity is the highest

Metals have a higher reflectance that the previous materials due to a higher extinction coefficient. The influence of the surface structure, i.e., of the dihedral angle of cavity, is consequently lower than for black glass and silicon, but remains comparable. For gold, the Fresnel reflectance depends on the wavelength of light, being much higher for long wavelengths than for short wavelengths. This is at the origin of the intense yellow color displayed in case of small dihedral angles. The color variations concern the chroma rather than the lightness. Comparable effects are observed with copper. For achromatic metals with high reflectance, the attenuation of light at each reflection is low, and the number of reflections as a weak impact on the amount of light that exits the cavity: the reflectance is very high in every observation direction. This is especially true for silver, whose reflectance, near 1, looks constant over the whole hemisphere. With aluminum, an attentive observation of the maps allows to distinguish the effect of the dihedral angle of cavity, which is similar to the one observed with the other metals.

4.3 Bi-hemispherical reflectance

The bi-hemispherical reflectance corresponds to a measurement geometry where the sample is illuminated by Lambertian light, and the reflected light is collected all over the hemisphere. It is obtained by integrating over the hemisphere the angular reflectance given by Eq. (37).

The irradiance on the structured surface is related to the radiance L_i according to the equation:

$$E_i = \int_{\theta=0}^{\pi/2}\int_{\varphi=0}^{2\pi} L_i \cos\theta \sin\theta d\theta d\varphi = \pi L_i \qquad (39)$$

and the flux reflected by a band of area $2\sin(\alpha/2)\Delta x$ on the surface is given by Eq. (35). The exitance is the sum of the reflected radiances expressed by Eq. (37):

$$M = \int_{\theta_r=0}^{\pi/2}\int_{\varphi_r=0}^{2\pi} L_r(\theta_r,\varphi_r)\cos\theta_r \sin\theta_r d\theta_r d\varphi_r \qquad (40)$$

Finally, the bi-hemispherical reflectance is given by:

Table 1 – Bi-hemispherical reflectance at 550 nm (in %)

Material	Dihedral angle of the V-cavity					
	45°	60°	90°	120°	150°	180°
Black glass	0.9	1.6	3.5	5.5	7.3	8.6
Silicon	11.0	16.6	26.4	34.0	36.8	37.3
Gold	66.3	72.9	80.0	83.6	85.1	85.4
Silver	89.7	92.1	94.4	95.6	96.0	96.1
Copper	33.9	42.8	54.4	61.2	63.9	64.6
Aluminum	77.1	82.2	87.4	90.2	91.0	90.9

$$\bar{R} = \frac{M}{E_i} = \frac{1}{\pi L_i}\int_{\theta_r=0}^{\pi/2}\int_{\varphi_r=0}^{2\pi} L_r(\theta_r,\varphi_r)\cos\theta_r \sin\theta_r d\theta_r d\varphi_r \qquad (41)$$

which yields, according to Eqs. (36) and (37),

$$\bar{R} = \frac{1}{2\pi\sin(\alpha/2)} \times \int_{\theta_r=0}^{\pi/2}\int_{\varphi_r=0}^{2\pi}\int_{y_p=-\sin(\alpha/2)}^{\sin(\alpha/2)} R(\theta_r,\varphi_r,y)dy_p \cos\theta_r \sin\theta_r d\theta_r d\varphi_r \qquad (42)$$

Using Eq. (42) with $R(\theta_r,\varphi_r,y)$ predicted by the rigorous model, we computed the spectral bi-hemispherical reflectances for the same dihedral angles of cavity and materials as in Fig. 6. The values at one wavelength, 550 nm, are presented in Table 1.

The spectral bi-hemispherical reflectances obained for a chromatic metal, namely gold, are shown also in Fig. 7. Each of them is then converted into color values in the CIE1976 L*a*b* color values. Its lightness L^*, and chroma C^* given by

$$C^* = \sqrt{a^{*2} + b^{*2}} \qquad (43)$$

are represented by a point in a (L^*, C^*) diagram on the right of the figure. All these values and spectra confirm the tendencies featured by the color maps shown in Fig. 6: As the dihedral angle decreases, reflectances also decrease and the surface has a darker appearance, because of a higher number of light reflections in the cavity which provokes more successive attenuations. Of course, this attenuation effect is stronger at wavelengths for which the material is less reflective or more absorbing, which explains that cavities with a smaller dihedral angle exhibit a more chromatic color, chroma being generally correlated with the contrast between highest and smallest reflectance values in the visible spectrum of light. This is clearly visible in the picture of Fig. 4.

Remind that the fact that the surface looks darker with smaller dihedral angles of cavity has nothing to do with shadowing or masking

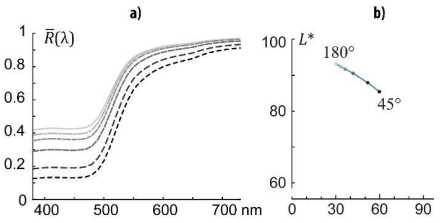

Fig. 7 – (a) Spectral bi-hemispherical reflectances of cavities with different dihedral angles made of gold, and (b) corresponding color components represented in the (L^*, C^*) diagram of the CIE1976 L*a*b* color space, predicted by the rigorous model for various of cavity.

effects, widely used in models for light scattering by rough surfaces [26]. In our models, shadowing is implicitly but rigorously taken into account, as all possible ray paths are considered from their entrance to their exit of the cavity. With facets of reflectance 1, all rays would exit the cavity and the bi-hemispherical reflectance would be 1.

4.4 Comparison between the rigorous and approximate models

In order to see how much the approximate models presented in Sections 3.1 and 3.2 deviate from the rigorous model presented in Section 3.3, we propose to compare reflectance maps, colors and lightness values predicted by the three models, for a selection among the materials and dihedral angles of cavity considered in Fig. 6 by favoring the ones which exhibit the highest differences. In Fig. 8, the hemispherical-directional reflectance maps are shown for silicon at a dihedral angle of 45°. There is a sensible difference between the three models for observation in the direction of the ridge (φ around 90°): The rigorous model predicts a darker color in this case.

In Fig. 9, the lightness profile of these three maps are compared along the horizontal diameter of the maps (observation perpendicular to the ridge, i.e., $\varphi = 0$ or π) and their vertical diameter (observation parallel to the ridge, i.e., $\varphi = \pi/2$ or $3\pi/2$). The difference between the rigorous model and its two approximate versions is once again well visible, except in graph a) where the rigorous and 2nd approximate model are equivalent when $\varphi = 0$: all multiple reflections occur in the same incidence plane, therefore the *p*-polarized component remains *p*-polarized and the *s*-polarized component remains *s*-polarized all along the multiple reflection process. In graph b), however, the three models differ dramatically. The fact that the lightness approached 0 near 63° is due to the fact that light strikes a facet with an incident angle near the Brewster angle while being almost totally *p*-polarized, which can be rendered only by the rigorous model, not the approximate ones. Comparable differences are obtained with gold, as well as the other materials, although it is less visible (color maps not reproduced here).

Finally, in Table 2, we compare, using the CIE1994 ΔE metric, the color differences associated with the bi-hemispherical reflectances predicted by the rigorous and the first approximate models for various materials, once again according to the dihedral angle of cavity. The color differences are very small for most materials, except at small dihedral angles of cavity for silicon, the material for which we have shown that the differences between the different models are the more pronounced. For this material, we also compare the colors issued from the rigorous and second approximate model, the deviations being even higher than the ones observed between the rigorous and first approximate model. For the other materials, and other angles for the silicon, the colorimetric distance CIE 1994 is lower than 1 unit, therefore almost non distinguishable.

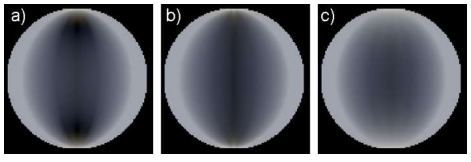

Fig. 8 – Color maps of the hemispherical-directional reflectance thanks to the Lambert azimuthal equal area projection, generated for silicon, with a dihedral angle of cavity of 45°, by using a) the rigorous model taking into account the polarization of light, b) the first approximate model assuming that light remains unpolarized after each reflection, and c) the second approximate model where the *p*- and *s*-components are assumed to be multiply reflected in parallel, independently from each other.

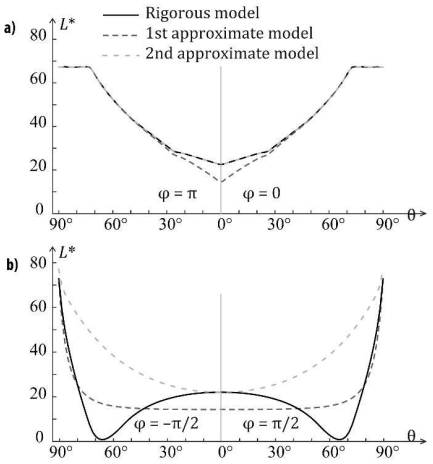

Fig. 9 – Lightness L^* in the CIE1976 L*a*b* color space computed from the spectral reflectance of silicon according to the rigorous model and the two approximate ones for a dihedral angle of cavity of 45°, as a function of the polar observation angle θ when (a) the observation direction is perpendicular to the ridges ($\varphi = 0$ or π) and (b) when it is parallel to the ridges ($\varphi = \pi/2$ or $3\pi/2$). These curves correspond to Lightness profiles of the (a) horizontal diameter and (b) vertical diameter of the maps shown in Fig. 8.

Table 2 – CIE 1994 ΔE values between colors corresponding to spectral reflectances predicted by different models

Material[a]	Dihedral angle of the V-cavity					
	45°	60°	90°	120°	150°	180°
Black Glass[a]	0.28	1.01	1.02	0.24	0.37	0.00
Gold[a]	0.39	0.55	0.43	0.13	0.15	0.00
Copper[a]	0.52	0.53	0.41	0.56	0.62	0.00
Silicon[a]	2.50	2.78	2.21	0.44	0.71	0.00
Silicon[b]	6.16	4.62	2.72	1.19	1.45	0.00

[a] ΔE value computed between the colors corresponding to the spectral reflectances predicted by the rigorous and 1st approximate models;
[b] ΔE value computed between the colors corresponding to the spectral reflectances predicted by the rigorous and 2nd approximate models

Table 3 – Bi-hemispherical reflectance (in %) at 550 nm of a V-cavity made of silver

Number of reflections taken into account	Dihedral angle of the V-cavity		
	45°	60°	90°
1	13.4	24.3	54.7
2	39.0	66.7	94.4
3	71.3	92.1	
4	89.7		

We would like to insist on the necessity to take all reflections of light into account, even though it is often assumed, especially in computer graphics, that one or two reflections suffice to obtain accurate or physically realistic color rendering of a structured surface. Table **3** illustrates the difference between bi-hemispherical reflectances that we would obtain by considering only the rays being reflected once within the cavity (the other rays being assumed to be blocked by a

neighboring facets therefore ignored), or the rays being reflected once or twice, or rays reflected up to three times, and finally the rays reflected up to four times, for a cavity made of silver at 550 nm (n = 0.1249 + i3.3391), silver being a highly reflective material. The reflectance values in the table are significant enough to show that it is crucial to account for all reflections, as recent studies in computer graphics also noticed, even though they used a model comparable to the one that we call here the first approximate model [10-11].

5. Conclusions

In this paper, we analyzed the interreflections occurring in a structured surface made of parallel V-cavities, with flat and mirror-like faces under a Lambertian illumination. We proposed a model taking into account the exact number of light reflections occurring in the structures, in order to accurately predict the reflectance according to the observation angle. We showed that the type of material and the dihedral angle of the cavity have a strong impact on the predicted reflectance, in particular because of the number of light reflections and the successive attenuations undergone by each ray according to the Fresnel coefficients. This is especially true for surfaces presenting concavities with a small dihedral angle: their color is darker, and in the case of chromatic materials such as gold and copper, their chroma strongly increases, even dramatically in some observation directions.

We also proposed to accurately take into account the change of incidence plane at each reflection of the light, inducing a change in its polarization, and therefore in the reflectance of the surface. We compared this rigorous approach with two approximate versions of the model which are simpler and faster to computed, the first one being comparable to the one that has been recently introduced in computer graphics [10-11]. The bi-hemispherical spectral reflectance computed with these three models are very close from each other, except for silicon when the dihedral angle of cavity is small. However, the hemispherical-directional reflectances predicted by the approximate models can deviate considerably from the one predicted by the rigorous model at some observation angles, especially those for which it is probable that light has become linearly polarized during its path before striking the next facet at an angle close to the Brewster angle.

As ridged surfaces are rather frequent in manufacturing (e.g. brushed steel objects), there is an interest in predicting accurately their appearance, in particular with prototyping renderers developed by the computer graphics community. Although this study has focused on an ideal special kind of ridged surface, perfectly periodical, the influence of the number of reflections and the polarization of light stands for every patterned surface. Several extensions of this theoretical study would be needed to see to which extent the color variations predicted according to the observation angle remains similar when the ridged surfaces is made of cavities with different dihedral angles, or when their facets are imperfect mirrors (non-flat, slightly scattering…) We can expect that these color variations are smaller than the ones drawn in this study, but follow similar tendencies. Moreover, as scattering tends to decrease the effect of polarization of light, we can expect that the difference between the rigorous polarization model and the first approximate one, which assumes that light remains unpolarized during the multiple reflection process, decreases. But this still needs to be shown.

Acknowledgement. This work was supported by Agence Nationale de la Recherche (ANR) through the grants ANR-15-CE38-0005 "MATERIAL", ANR-10-LABX-0075, and ANR-11-IDEX-0007.

References

1. S. Kinoshita, S. Yoshioka and J. Miyazaki, "Physics of structural colors", *Reports on Progress in Physics*, 71 (2008).
2. R. Charrière, G. Lacaille, M. Pedeferri, J. Faucheu, D. Delafosse, "Characterization of the gonioapparent character of colored anodized titanium surfaces". *Color Res. Appl.* **40**, 483–490 (2015).
3. P. Kubelka, "New contributions to the optics of intensely light-scattering material, part I," *J. Opt. Soc. Am. A* **38**, 448–457 (1948).
4. N. T. Melamed, "Optical properties of powders: Part I. Optical absorption coefficients and the absolute value of the diffuse reflectance," *J. Appl. Phys.* **34**, 560–570 (1963).
5. S. Chandrasekhar, *Radiative Transfer* (Dover, 1960).
6. H. C. van de Hulst, *Light Scattering by Small Particles,* Dover, pp. 200–227, 1981.
7. P. Beckmann and A. Spizzichino, *The scattering of electromagnetic waves from rough surfaces,* MA Artech House INC, Norwood, pp. 70–98, 1963.
8. K.E. Torrance, E.M. Sparrow, "Theory for off-specular reflection from roughened surfaces," *J. Opt. Soc. Am.* **57**, 1105–1114 (1967).
9. E. Heitz, J. Hanika, E. d'Eon, and C. Dachsbacher, "Multiple-Scattering Microfacet BSDFs with the Smith Model," ACM Trans. Graph. (Proc. SIGGRAPH 2016) **35**, Article 58 (2016).
10. F. Xie, P. Hanrahan, "Multiple scattering from distributions of specular v-grooves," ACM SIGGRAPH Asia 2018 Technical Papers, Article 276 (2018).
11. 1.10. J.H. Lee, A. Jarabo, D.S. Jeon, D. Gutierrez, M.H. Kim, "Practical multiple scattering for rough surfaces," ACM SIGGRAPH Asia 2018 Technical Papers, Article 275 (2018).
12. P. Kubelka, "New contributions to the optics of intensely light-scattering materials, part II: Non homogeneous layers", *J. Opt. Soc. Am. A*, **44**, 330–335, (1954).
13. L. Simonot, M. Hébert, R.D. Hersch, "Extension of the Williams-Clapper model to stacked nondiffusing colored coatings with different refractive indices," *J. Opt. Soc. Am. A* **23**, 1432–1441 (2006).
14. M. Hébert, R.D. Hersch, J.-M. Becker, "Compositional reflectance and transmittance model for multilayer specimens," *J. Opt. Soc. Am. A* **24**, 2628–2644 (2007).
15. P. Emmel and R.D. Hersch, "A Unified Model for Color Prediction of Halftoned Prints," *J. Im. Sci. Technol.*, **44**, 351–359, (2000).
16. F.R. Clapper and J.A.C. Yule, "The Effect of Multiple Internal Reflections on the Densities of Halftone Prints on Paper", *J. Opt. Soc. Am.* **43**, 600–603 (1953).
17. J.A.C. Yule and W.J. Nielsen, "The penetration of light into paper and its effect on halftone reproductions", *Proc. TAGA* **3**, 65–76 (1951).
18. G. Rogers, "Effect of light scatter on halftone color", *J. Opt. Soc. Am. A* **15**, 1813–1821 (1998).
19. G. Rogers, "A Generalized Clapper-Yule Model of Halftone Reflectance", *Color Res. Appl.* **25**, 402–407 (2000).
20. D. Saint-Pierre, R. Deeb, D. Muselet, L. Simonot, M. Hébert, "Light Interreflections and Shadowing Effects in a Lambertian V-Cavity under Diffuse Illumination" IS&T Electronic Imaging Symposium, Material Appearance (Burlingame, USA, 29 January-2 February 2018).
21. R. Deeb, D. Muselet, M. Hebert, A. Trémeau, "Spectral reflectance estimation from one RGB image using self-interreflections in a concave object". *Appl. Opt*. **57**, 4918-4929 (2018).
22. D. Saint-Pierre, L. Simonot, M. Hébert, "Reflectance computation for a specular only V-cavity" International Workshop on Computational Color Imaging. Springer, Cham, 289-303 (2019).
23. M. Born and E. Wolf, *Principle of Optics*, 7th expanded ed., Pergamon, 1999, p. 47.
24. Nicomedus, F.E., Richmond, J.C., Hsia, J.J., "Geometrical considerations and nomenclature for reflectance," NBS Monograph 160, NBS, 52 (1977).
25. JP. Snyder, *Map Projections – A Working Manual,* U. S. Geological Survey Professional Paper 1395; U. S. Government Printing Office, Washington, DC, 182–190 (1987).
26. B.J. Smith, "Geometrical shadowing of a random rough surface," *IEEE Transaction on Antennas and Propagation*, **15**, 668–671 (1967).